Aramid Nanofiber Membranes for Energy Harvesting from Proton Gradients

Cheng Chen, Guoliang Yang, Dan Liu,* Xungai Wang, Nicholas A. Kotov,* and Weiwei Lei*

Harvesting osmotic energy from industrial wastewater is an often-overlooked source of electricity that can be used as a part of the comprehensive distributed energy systems. However, this concept requires, a new generation of inexpensive ion-selective membranes that must withstand harsh chemical conditions with both high/low pH, have high temperature resilience, display exceptional mechanical properties, and support high ionic conductance. Here, aramid nanofibers (ANFs) based membranes with high chemical/thermal stability, mechanical strength, toughness, and surface charge density make them capable of high-performance osmotic energy harvesting from pH gradients generated upon wastewater dilution. ANF membranes produce an averaged output power density of 17.3 W m^{-2} for more than 240 h at pH 0. Taking advantage of the high temperature resilience of aramid, the output power density is increased further to 77 W m^{-2} at 70 °C, typical for industrial wastewater. Such output power performance is 10× better compared to the current state-of-the-art membranes being augmented by Kevlar-like environmental robustness of ANF membranes. The improved efficiency of energy harvesting is ascribed to the high proton selectivity of ANFs. Retaining high output power density for large membrane area and fluoride-free synthesis of ANFs from recyclable material opens the door for scalable wastewater energy harvesting.

1. Introduction

Harvesting of osmotic energy (sometimes also referred to as blue energy),[1] is typically realized as geotechnical projects using dykes dividing fresh and salty water bodies using

pressure-retarded osmosis (PRO) for water molecules moving into driving energy and reverse electrodialysis (RED) for converting transmembrane ion transport into electric current.[2–5] Large capital cost and low efficiency of both PRO and RED impede their implementation.[6,7] However, the same principle of energy generation can be utilized in a different setting with industrial wastewaters. The aqueous industrial discharge often has high concentrations of various inorganic ions (Li$^+$, Na$^+$, K$^+$, Cl$^-$, SO$_4^{2-}$, H$_2$PO$_4^-$) and extreme pH values,[8,9] which requires gradual neutralization and dilution to mitigate environmental harm.[10,11] Both chemical processes can generate osmotic energy when realized across osmotic membranes and high ionic content is conducive to high power output.[12,13] Also important that osmotic dilution can be realized without additional CO$_2$ emission.

However, this concept is difficult to bring to fruition because of the lack of appropriate ion selective membranes. They need to display uncommon chemical resistance to operate in extreme pH environments. Simultaneously, these membranes must also have high ionic selectivity, ionic conductivity, temperature resilience, and mechanical strength. A large spectrum of nanoporous membranes were prepared using composite materials based on graphene oxide,

C. Chen, G. Yang, D. Liu, X. Wang, W. Lei
Institute for Frontier Materials
Deakin University
Locked Bag 2000, Geelong, Victoria 3220, Australia
E-mail: dan.liu@deakin.edu.au; weiwei.lei@deakin.edu.au
C. Chen
School of Resources and Environment
Anhui Agricultural University
130 Changjiang West Road, Hefei, Anhui 230036, China
N. A. Kotov
Department of Chemical Engineering
University of Michigan
Ann Arbor, MI 48109, USA
E-mail: kotov@umich.edu

N. A. Kotov
Department of Biomedical Engineering
University of Michigan
Ann Arbor, MI 48109, USA
N. A. Kotov
Department of Materials Science and Engineering
University of Michigan
Ann Arbor, MI 48109, USA
N. A. Kotov
Biointerfaces Institute
University of Michigan
Ann Arbor, MI 48109, USA

clay, boron nitride, MXenes, molybdenum disulfide (MoS$_2$), and silk.[14–21] Their applicability to energy harvesting from wastewater is impeded, however, by the lack some of these materials properties. The mechanical properties, ion flux and pH resilience typically suffer when sufficient ion selectivity is achieved. The building blocks of currently known nanoporous membranes react with the electrolytes in extreme pH gradients and disaggregate.[22] For wastewater treatment technologies, the cost of the high-performance composites can be another valid concern.[14,20]

Aramid nanofibers (ANFs), a new "nanoscale building block", have outstanding mechanical properties and abundant surface charge groups, which make them ideal for nanocomposite membranes. ANFs have similarities with nanowires, cellulose nanofibrils, and carbon nanotubes but display unique branched morphology that affords an opportunity to create intricately interdigitated fibrous networks.[23,24] ANFs-based materials have been applied in many fields, such as supercapacitor electrodes, dendrite-suppressing ion conductors, lithium ion batteries, nanofiltration membranes, and electrical heaters.[23,25–28] The recent ANF-boron nitride (ANF-BN) nanocomposite membranes showed excellent osmotic energy harvesting performance under wide thermal ranges.[29] Moreover, Zhang et al. recently reported that their ANFs-MXene nanocomposite membranes can be used for osmotic energy conversion with a power density of 4.1 W m^{-2} with sea water and river water,[30] which is close to the commercial osmotic energy conversion goal of 5 W m^{-2}.[31] However, the stability of components (such as, MXenes) membranes will limit their application in case of corrosive electrolyte solutions, especially industrial wastewater with high acidity. Therefore, mechanical and chemically resistant ANF membranes open the door for energy harvesting from wastewaters even when they possess extremely low pH values.

Here we show that ANF membranes can be used to harvest energy from proton concentration gradients, which in large part replicates the functionality of many biological membranes. The ANF membranes showed exceptional mechanical properties and excellent stability even in hydrochloric acid (HCl) solutions with concentration between 0.001 and 1 M with pH as low as 0. The ANF membranes showed averaged output power density of 17.3 W m^{-2} and excellent stability for more than 240 h in a 1 M HCl solution due to high cation selectivity and rapid transport of protons through hydrogen-bonded networks. Further improvement of osmotic energy harvesting performance can be attained by increasing the temperature to reach one order of magnitude greater performance.[32]

2. Results and Discussion

The ANFs, 10 ± 3 nm in diameter and several microns in length (Figure S1, Supporting Information), are produced by controlled hydrolysis of aramid microscale fibers in dimethyl sulfoxide (DMSO) (see Methods). The process is suitable for the up-cycling of aramid fabrics manufactured for a variety
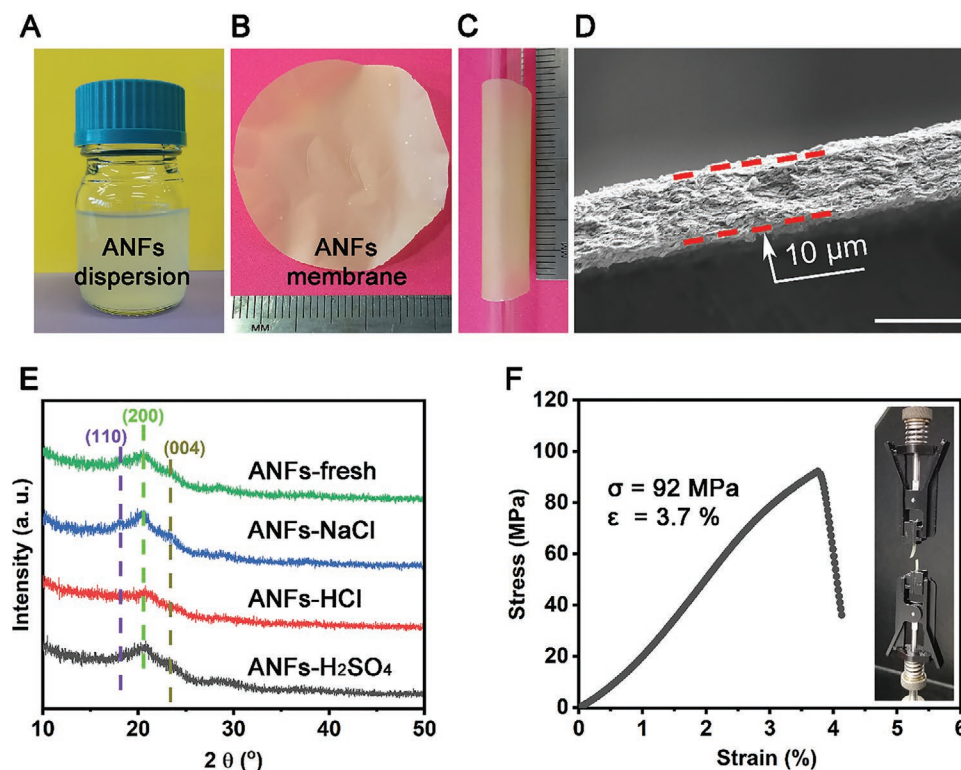
Figure 1. Fabrication and characterization of ANF membranes. A) Photograph of the ANF dispersion in water. B) Photograph of the ANF membrane. C) The ANF membrane wrapped around a glass tube. D) Cross-sectional SEM image of the ANF membrane. E) XRD patterns of the ANF membrane after treatments of different solutions for 24 h. F) Mechanical property measurement of the ANF membrane. The scale bar is 10 μm in (D). The membranes that we used here had a thickness of 10 μm.

of applications. After removing the DMSO, the ANF dispersion was magnetically stirred in an aqueous 0.1 KOH solution (**Figure 1**A). The aqueous ANFs dispersion was vacuum-filtered through a nylon membrane to obtain the ANF membrane with desired thickness. The freestanding ANF membranes were then easily peeled off the nylon membrane by wetting it with one drop of water (Rehbinder effect) after drying at 60 °C for 1 h (Figure 1B,C). The scanning electron microscope (SEM) image showed that the surface of the ANF membrane was flat (Figure S2, Supporting Information) and the thickness of the membrane was uniform (Figure 1D). While the parent aramid is hydrophobic, the ANF surface has carboxyl, hydroxyl, and amino groups, which impart the membrane with charge and strong non-covalent bonding between the neighboring ANFs via hydrogen bonds.[24] These chemical and nanoscale structure endowed the ANF membranes with excellent mechanical performance reminiscent of silk fibersand cartilage.[21,33–35]

X-ray diffraction (XRD) patterns of ANF membranes show peaks at (110), (200), and (004) (Figure 1E). The wide diffraction peak (23.0°) is due to deconstruction of the crystalline structure of the aramid.[36] To further study the chemical stability of the ANF membrane in different solutions, the ANF membranes were soaked in target solutions for one week and then dried, and their structure examined using XRD (Figure 1E). The ANF membranes showed similar XRD patterns even after being soaked in HCl (1 M), H_2SO_4 (1 M), and NaCl (1 M), respectively (Figure 1E and Figure S3, Supporting Information). There was no change of the peak positions in the XRD patterns, confirming the chemical stability of the ANF membranes. The stability of ANF membrane in these chemically aggressive conditions was further confirmed by Fourier transformed infrared (FTIR) and Raman spectra (Figures S4 and S5, Supporting Information).

The tensile stress–strain curves of the ANF membranes (2.5 mm × 12 mm) showed a strength of 92 MPa (Figure 1F) and Young's modulus of 2.48 GPa. The mechanical strength of the ANF membranes is notably higher than other nanocomposite membranes,[37–39] which is associated with the highly interconnected percolating network and extensive hydrogen bonding between neighboring ANFs in the membrane.[40,41]

The ion-transport properties of the ANF membranes were investigated by ionic current–voltage (I–V) measurements using an electrochemical device (IviumStat analyzer).[42] The ANF membrane was mounted in H-cells filled with 12 mL of target solution for each test (**Figure 2**A). Using HCl as an example, the current showed a positive relationship to the applied voltage (from −0.2 to + 0.2 V). When the concentration of HCl ranged from 10^{-6} to 1M, the current significantly increased with applied voltage. The calculated ionic conductivity follows the bulk values in high concentration region (>0.1 M) and gradually deviates from bulk value in low concentration region (<0.1 M) (Figure 2B), which is similar for other membranes.[18,30] Cumulatively, these data sets imply that the hydrophilic ANF membrane can enhance the conductance of ions through the nanoscale pores with an electric double layer in low concentrations.[24]

To understand the ionic transport with concentration gradients, the ANF membranes were tested in an H-cell with asymmetric electrolytes (Figure 2C). Using HCl as an example, both H^+ and Cl^- ions were driven in the same direction with the
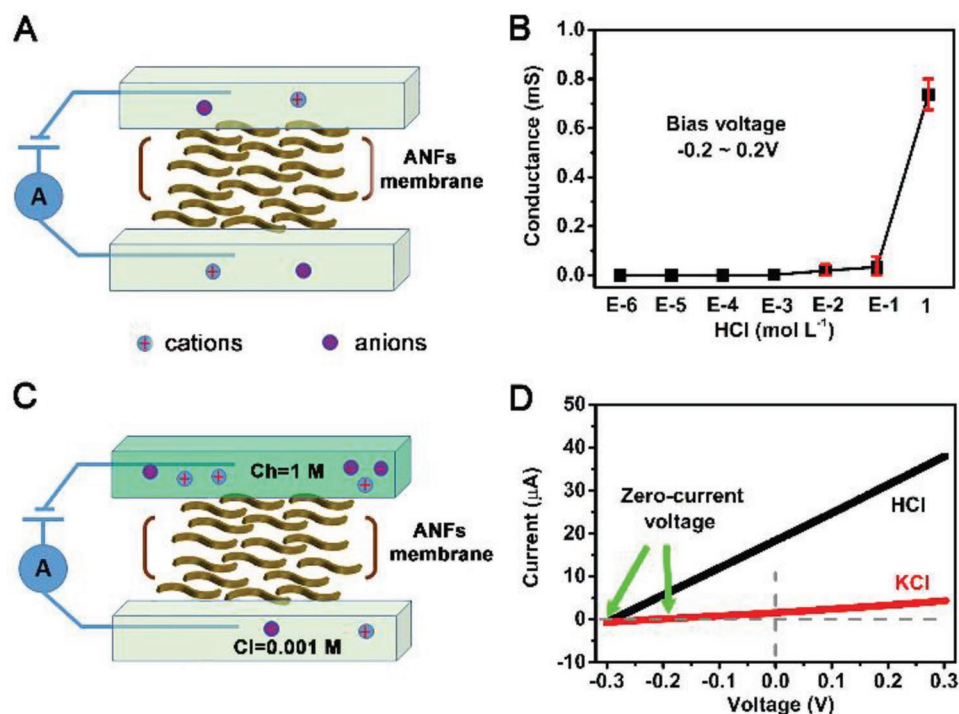
Figure 2. Ion transport and selectivity across the ANF membrane. A) Schematic of an ANF membrane in HCl with constant concentration. B) Conductance observed for ANF membranes in HCl with constant concentration. C) Schematic of an ANF membrane in HCl with concentration gradient. D) I–V curves for HCl and KCl in the two reservoirs connected by ANF membranes. Note: For (C,D), HCl and KCl solutions were prepared with Ch = 1 M; Cl = 0.001 M, separately.

ADVANCED
SCIENCE NEWS
www.advancedsciencenews.com

ADVANCED
FUNCTIONAL
MATERIALS
www.afm-journal.de

concentration gradient osmotic pressure, from the high concentration (C_h) reservoir to the low concentration (C_l) reservoir. Importantly, the sign of the electric current, I, at zero applied voltage indicates whether most carriers are H$^+$ or Cl$^-$.[43,44] The current at zero voltage was positive, indicating that the proton transport drives the system to balance in the two reservoirs. We noted that the zero-current voltage actually consists of two parts: 1) the diffusion potential (E_{diff}), which is created by the power source, and 2) the redox potential (E_{redox}), generated by the unequal potential drop at the electrode solution interface.[42] We can clearly see that the cations are the charge carriers through the ANF membranes, which is consistent with their negatively charged surface (Figure S6, Supporting Information). Furthermore, the proposed voltage caused by the concentration gradient can be calculated by the Nernst equation:[22,39]

$$V_{osmotic} = s \frac{RT}{F} \ln \frac{C_{max}}{C_{min}} \tag{1}$$

where s is the transport number for cations (t^+) or anions (t^-) ranging from 0 to 1, T is the temperature (298.0 K), and R is the gas constant (8.314 J k^{-1} mol^{-1}), and F is the Faraday constant (96,500 C mol^{-1}), C_{max} is the high concentration while the C_{min} is the lower concentration part. When assuming the total ion transport factor $t^+ + t^- = 1$, we can get the transport numbers for H$^+$ ($S_H = 0.838$) and K$^+$ ($S_K = 0.616$) (Table S1, Supporting Information). This means that the H$^+$ showed higher transport number compared to K$^+$, making it possible to get improved osmotic energy harvesting from the HCl solutions.[45]

The ion selective membranes highlight the potential of using ionic current for energy harvesting from pH gradients. Prior studies of atomically thin micas showed nearly perfect proton selectivity in HCl solutions,[44–46] but only in the direction parallel to the atomic layer. Practical aspect of energy harvesting, however, requires similarly ideal behavior in for ion transport perpendicularly to membrane surface.

To understand better the prospects of ANF membranes for proton gradient-induced power generation, they were tested in solution pairs with various acidity.[14,20] The measured ideal energy generation of the membrane can be calculated from the short circuit current (I_{SC}) timing of the measured voltage ($V_{measured}$) after dividing four times of the working area. In the subsequent discussion, the osmotic power generation performance results were averaged over 4 h. The working area of ANF membranes used for the osmotic energy harvesting device is 0.03 mm^2, which is typical in the field.[30,31] When HCl (0.001 M) was selected as the low concentration (C_l) reservoir, the produced current and measured power density increased as the high concentration (C_h) reservoir increased from 0.01 to 1 M (**Figure 3**A). The produced I_{SC} ranged from 0.87 ± 0.08 (C_h (0.01 M)) to 7.6 ± 0.5 µA (C_h (1 M)), and the maximum measured power density is 19.5 ± 0.5 W m^{-2} (C_h (1 M)), which is sufficient for realistic osmotic energy generation in industrial settings.[11]

The size and chemical nature of the hydrated radius of cations affects the osmotic energy generation and must be evaluated because of the mixture of ions present in wastewater especially those with low pH. Selecting Cl$^-$ as a common anion, Li$^+$ (3.82 Å), Na$^+$ (3.58 Å), and K$^+$ (3.31 Å) were compared with H$^+$ (2.82 Å) (Figure 3B). The C_l and $C_h$ reservoirs were filled with 0.001 and 1 M solutions, respectively. The higher hydrated radii of the cations in chloride solution resulted in lower osmotic current and power generation compared to the proton concentration gradient. The LiCl solution showed a current of 0.57 ± 0.01 µA with a measured power density of 1.17 ± 0.01 W m^{-2}, which was much smaller than that for HCl. The NaCl and KCl solutions showed improved values of 1.83 ± 0.1 and 2.46 ± 0.25 W m^{-2}, respectively, but this is still far below what is required for practicality because of the low energy conversion efficiency. Similarly, H$^+$ was a control while SO$_4^{2-}$ (3.79 Å) and H$_2$PO$_4^{2-}$ (4.9 Å) were selected as anions (Figure 3C). HCl (C_h (1 M)/C_l (0.001 M)) with low hydrated anion and cation radii produced the optimized current (7.6 ± 0.5 µA) and power density (19.5 ± 20.5 W m^{-2}). The H$_3$PO$_4$ and H$_2$SO$_4$ showed measured power densities of 1.16 ± 0.03 and 1.24 ± 0.05 W m^{-2}, respectively. In short, cations moving across the membranes are beneficial for the produced voltage, and the anions with different radii and diffusion coefficient contribute to the improved current, leading to the increased concentration gradient energy power gernartion.[42] Besides having the smallest hydrated radii (2.82 Å), proton transport through ANF membranes is likely to be enhanced water hydrogen-bonded network along the surface of nanofibers.[47]

The current and power density variation over 24 h is a direct way to assess the stability of the energy generation performance (Figure 3D).[31] The current showed no change even after 24 h, starting from 308 to 310 mV, while the power density increased from 19.1 to 19.7 W m^{-2}. The stable voltage implies negligible polarization effect on the ANF membrane with the protons driving the system toward the equilibrium in an effort to equalize proton concentrations in the two reservoirs.[31,44] No degradation of power performance was observed between different cycles during the repeated tests for a total of 240 h (Figure 3E), highlighting the high stability of ANF membranes essential for the energy generation from wastewater.

When the active area decreased of ANF membranes from 78.5 to 0.03 mm^2, the produced current quickly declined from 228 to 7.6 µA, while the power density quickly increased from 0.16 to 19.6 W m^{-2} (Figure 3F).

The power generated across ANF membranes for external circuit needs to be maximized.[48] **Figure 4**A shows that the transmembrane voltage improves with increased external resistance. For HCl solution with C_h (1 M)/C_l (0.001 M), the output voltage (U) increased to 288 mV, which is close to the measured voltage (310 mV). Similarly, the H$_2$SO$_4$, H$_3$PO$_4$, and LiCl solutions followed such a trend with the increase of external resistance. The output electric power, (P), consumed on the resistor load (R) in the external circuit can be directly obtained by P = U^2/R.[49] With the increase of load resistance, the output power density reaches its peak value and then decreases to its lowest value (Figure 4B).[20,48] At the output power density peak, the external resistance implies the inner resistance of the ANF membranes in a given solution. Therefore, the inner resistance of ANF membranes is 47 kΩ in HCl, 200 kΩ in KCl, 100 kΩ in H$_2$SO$_4$, and 100 kΩ in H$_3$PO$_4$. Correspondingly, the output power density peak is 17.3 W m^{-2} for HCl, 2.35 W m^{-2} for KCl, 1.06 W m^{-2} for H$_2$SO$_4$, and 0.7 W m^{-2} for H$_3$PO$_4$ (Table S2, Supporting Information). The lowest inner resistance of ANF membranes in HCl solution accounts for the highest energy
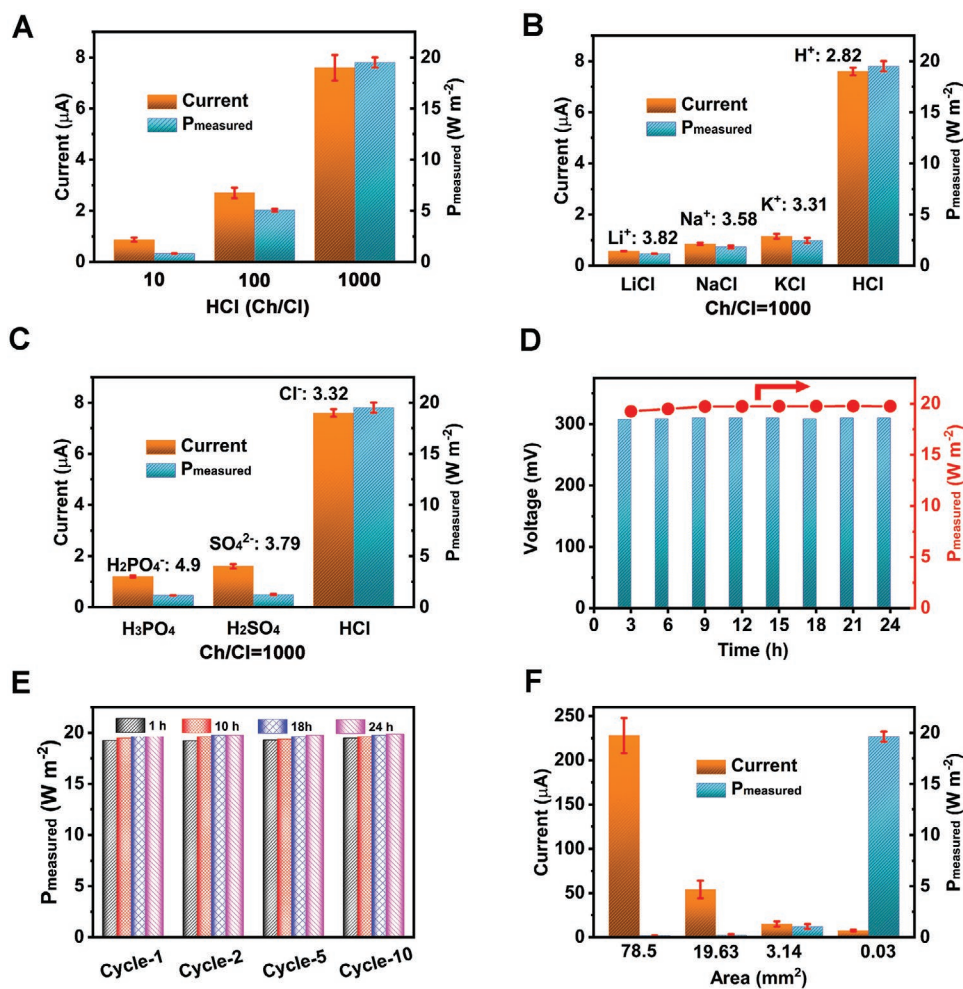
Figure 3. Temporal and areal dependence of the power generation from proton gradients across the ANF membranes. A) Generated current and ideal measured power density as a function of HCl concentration gradient. The Ch of the HCl was 1 M, while changing the Cl from 0.001 to 0.1 M. B) Generated current and ideal measured power density as a function of hydrated cations. C) Generated current and ideal measured power density as a function of hydrated anions. D) Dynamic generated voltage and ideal measured power density. E) Cycling performance of the ANF membrane. F) Comparison of working area of ANF membranes for generated current and measured power density. Note: For (B–F), all of the test solutions were controlled with Ch = 1 M and Cl = 0.001 M. The ideal salinity energy was calculated according to Equation (4).

harvesting from ion transport. Even through the output power density is much higher than the practical request (5 W m^{-2}), the osmotic energy part was 3.4 W m^{-2} with HCl as electrolyte (Table S3, Supporting Information). Furthermore, to prove the excellent stability of the ANF on concentration energy outputting from the simulated wasted acid, an external resistor with fixed resistance equaling to the inner resistance of the device was connected with the device without disconnection for 12 h (Figure S7, Supporting Information).

The comparison of various nanoporous membranes with different working areas for energy output can be found in Table S4, Supporting Information.[14,16,20,30,31,50–54] One can observe that reduction of membrane area leads to high output power density, for example, for membranes from BN nanotubes (4 kW m^{-2}) and MoS$_2$ (10^6 W m^{-2}).[14,20] When the working area of the membranes increased, the osmotic energy output drops and hovers ≈5 W m^{-2}, for example for ANF-MXene (4.1 W m^{-2}) and Janus membranes (5.1 W m^{-2}).[30,31] The output power density of the

ANF membrane is 17.3 W m^{-2}, which is much higher than other membranes with the same active area (3 × 10^4 μm^2). While in the centimeter region,[54,55] the power density was ≈1 W m^{-2}. These results are informative for understanding the effect of working area of membranes on osmotic energy harvesting and comparative performance of different materials designs.

Measurements were carried out on ANF membranes with C_h (1 M)/C_l (0.001 M) heated in an oil bath.[29] For every test, the oil bath was first heated to a target temperature and then the transferred voltage on the external resistance was recorded. Figure 4C,D shows the output voltage and power increase with the temperature increases, indicating the thermal stability of ANF membranes. When the temperature was increased to 70 °C (343 K), the maximum output voltage reached 378 mV and the corresponding output power density was 77 W m^{-2} (Table S5, Supporting Information). Both of these values are an order of magnitude higher than many membranes.[30,31] Such an unexpected increase is associated with proton transport via
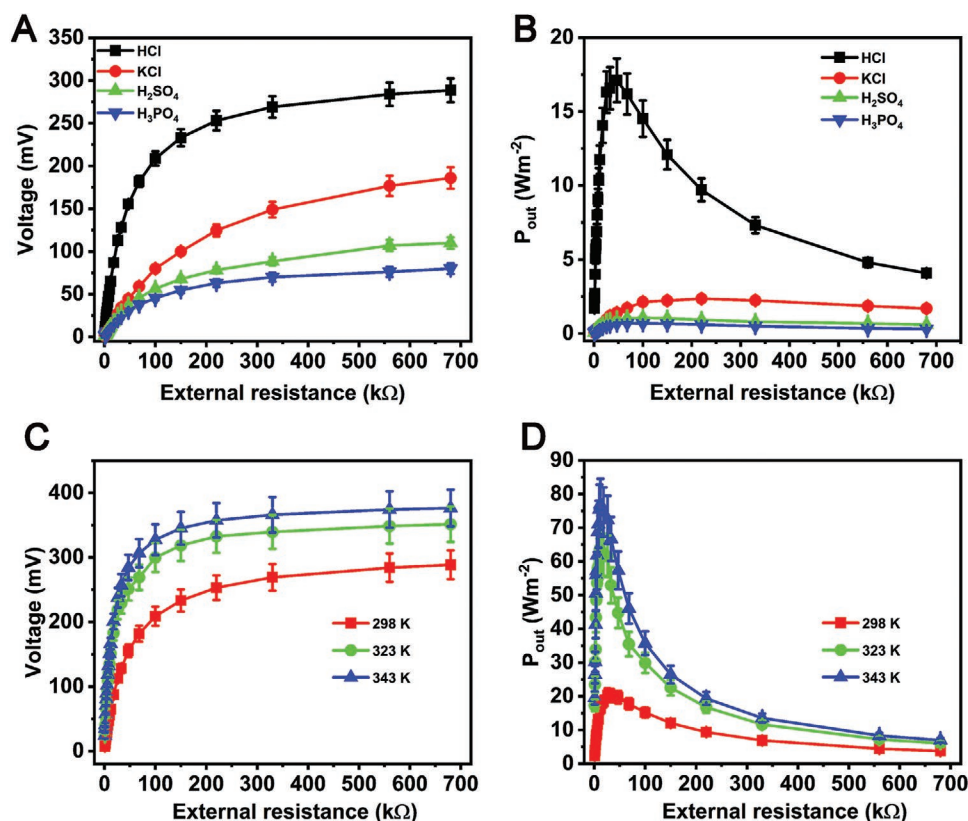
Figure 4. Power output for energy generation across the ANF membranes for different ions and temperatures. A) The voltage output versus external resistance in HCl, KCl, H_2SO_4, and H_3PO_4, respectively. B) The output power density versus external resistance in HCl, KCl, H_2SO_4, and H_3PO_4, respectively. C) The voltage output versus external resistance in M HCl with different temperature. D) The output power versus external resistance in HCl with different temperature. Note: All of the testing solutions were controlled with Ch = 1 M and Cl = 0.001 M.

Grotthuss mechanism and can further extend the high temperature applications of ANF membranes.[18,47,56]

The power and voltage of energy harvesting from wastewater can be further modulated as needed using series and parallel connections of multiple devices (**Figure** 5A,B).[16] When the two H-cells are connected in series, the measured potential, $V_{measured}$, can be increased to 0.6 V. Similarly, the produced current can be doubled to 15.1 µA when the two H-cells were connected in parallel. In addition, voltage and current tests over 5 h demonstrated the temporal stability of the energy generators based on ANF membranes.

3. Conclusion

In conclusion, the unique combination of properties of ANF nanoporous membranes results makes it fundamentally possible to generate energy from wastewater using proton concentration gradient. The osmotic device harvested an average of 17.3 W m^{-2} power for more than 240 h without degradation even in 1 M HCl, considerably increasing to 77 W m^{-2} at 343 K common for industrial water discharge. Retaining high output power density for large membrane area and fluoride-free synthesis of ANF from recyclable materials brings extraction of the energy hidden in the wastewater a step closer to reality.

4. Experimental Section

Synthesis of ANF Dispersions: 1 g of Kevlar pulp was sheared into 1 cm fragments. Then, the aramid (Kevlar) cut microfibers and 1.5 gram potassium hydroxide (KOH) were added into 500 mL DMSO solution and stirred for 1 week at room temperature.[24] The resulting ANF dispersion showed a dark red color. The ANF solution is sensitive to water, so the solution must be free of water or moisture. Then the ANFs were washed with 4 L of DI water to remove all the DMSO solvent. The ANFs were then dispersed in 0.1 KOH solution for one week for further application.

Synthesis of ANF Membrane: The synthesis of ANF membrane with controllable thickness was prepared via the vacuum method. Typically, ANF membranes were assembled by vacuum filtration of the ANF dispersion through a Nylon membrane filter (25 mm diameter, 0.2 µm pore size, Whatman). To remove the KOH, 2 L of water was used to wash the ANF membrane through the vacuum setup. The ANF membrane can easily be peeled off with one drop of water from the filter after drying in oven for 1 h at 60 °C. The obtained thin membranes were light yellow and translucent, and could be easily cut into a desired shape and size using a razor blade. The thickness of prepared ANF membranes was 1–100 µm, and the ANF membrane with 10 µm was chosen, unless otherwise stated.

Material Characterization: The SEM analysis was performed on a Zeiss Supra 55 VP with a 5 nm carbon coating. XRD measurements were performed on a Panalytical X'Pert PRO apparatus with Cu Kα radiation. To see the stability of the ANF membranes, samples were soaked in solutions for one week and then characterized with XRD, FTIR (Nicolet 7199 FTIR), and Raman (514 nm, Ranishaw Raman) spectroscopy. To
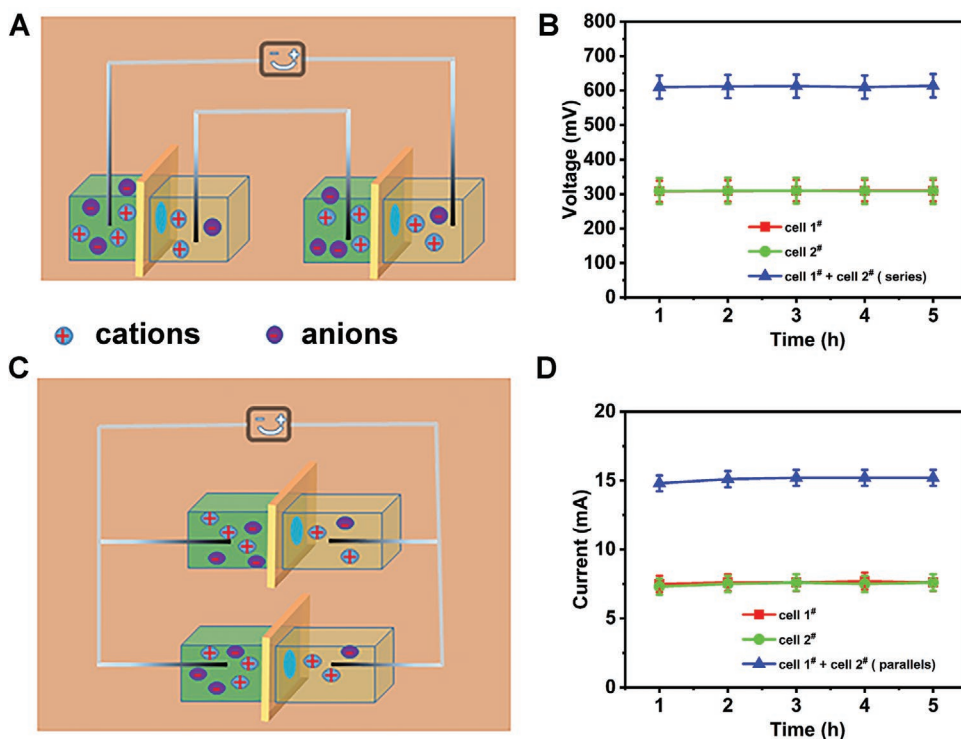
Figure 5. Operation of ANF cells in tandem devices. A) Schematics for two H-cells in series. B) The produced voltage with two cells in series. C) Schematics for two cells in parallel. D) The produced current with two cells in parallel. Note: HCl solutions with $C_h = 1$ M and $C_l = 0.001$ M were tested for the tandem measurement.

test the zeta potential, a 1 cm × 2 cm piece of ANF membranes was conducted on a SurPASS™ 3 with 0.1 M KCl as the electrolyte.

Mechanical Measurements: The mechanical performance of the ANF membranes with 2.5 mm wide to 12 mm long rectangular strip was evaluated with an Instron 5960 Series Tensile Tester (Instron Corporation). Three parallel tests were averaged to get the stress–strain curves at a rate of 10 mm min^{-1} with a ≈5 N range load cell. The stress (σ) of the ANF membranes was calculated using

$$\sigma = F/(a \times b) \tag{2}$$

where F is the loading force (N), a and b are the width (2.5×10^{-4} m) and thickness of the membranes (10×10^{-6} m), respectively. The strain (ε) was calculated using

$$\varepsilon = \Delta L/L \times 100\% \tag{3}$$

where ΔL is the change of membrane length, and L is the original membrane length (12×10^{-4} m).

Electrical Measurements: The ANF membrane was mounted between a custom-made two-compartment electrochemical cell. The working areas of the membranes were 3×10^4 μm^2, 3.14 mm^2, 19.625 mm^2, and 78.5 mm^2. Homemade Ag/AgCl electrodes were used to apply a transmembrane electrical potential. *I–V* curves of the ANF membranes were recorded at various electrolytes using an IviumStat analyzer. Then 12 mL of HCl, H$_2$SO$_4$, H$_3$PO$_4$, LiCl, NaCl, and KCl electrolyte of various concentrations were injected into each half-cell for osmotic energy harvesting measurements. The produced current and voltage values were recorded with a Keithley 6517B with a pair of Ag/AgCl electrodes. The measured power generation can be calculated using

$$P_{measured} = V_{measured} \times I_{measured}/4A \tag{4}$$

where $V_{measured}$ is the open-circuit voltage, $I_{measured}$ is the short-circuit current, and A is the working area of the ANF membrane for each test. For the output power measurements, the external resistances were tandem with the cells. The external load resistance output power can be calculated using

$$P_R = V_R^2/R \tag{5}$$

where V_R is the voltage on the external load, and R is the external load resistance.

Supporting Information

Supporting Information is available from the Wiley Online Library or from the author.

Acknowledgements

Conflict of Interest

The authors declare no conflict of interest.

Data Availability Statement

Keywords

[1] A. Siria, M.-L. Bocquet, L. Bocquet, *Nat. Rev. Chem.* **2017**, *1*, 0091.

[2] J. G. Hong, B. Zhang, S. Glabman, N. Uzal, X. Dou, H. Zhang, X. Wei, Y. Chen, *J. Membr. Sci.* **2015**, *486*, 71.

[3] M. Vanoppen, E. Criel, G. Walpot, D. A. Vermaas, A. Verliefde, *npj Clean Water* **2018**, *1*, 9.

[4] J. Veerman, M. Saakes, S. J. Metz, G. J. Harmsen, *Environ. Sci. Technol.* **2010**, *44*, 9207.

[5] Y. Mei, C. Y. Tang, *Desalination* **2018**, *425*, 156.

[6] N. Y. Yip, D. Brogioli, H. V. M. Hamelers, K. Nijmeijer, *Environ. Sci. Technol.* **2016**, *50*, 12072.

[7] A. P. Straub, A. Deshmukh, M. Elimelech, *Energy Environ. Sci.* **2016**, *9*, 31.

[8] S. De Gisi, M. Notarnicola, in *Encyclopedia of Sustainable Technologies*, (Ed: M. A. Abraham), Elsevier, Oxford **2017**, pp. 23–42.

[9] P. J. J. Alvarez, C. K. Chan, M. Elimelech, N. J. Halas, D. Villagrán, *Nat. Nanotechnol.* **2018**, *13*, 634.

[10] M. A. Shannon, P. W. Bohn, M. Elimelech, J. G. Georgiadis, B. J. Mariñas, A. M. Mayes, *Nature* **2008**, *452*, 301.

[11] D. S. Sholl, R. P. Lively, *Nature* **2016**, *532*, 435.

[12] S. Marbach, L. Bocquet, *Chem. Soc. Rev.* **2019**, *48*, 3102.

[13] C. F. Wan, T.-S. Chung, *J. Membr. Sci.* **2015**, *479*, 148.

[14] A. Siria, P. Poncharal, A.-L. Biance, R. Fulcrand, X. Blase, S. T. Purcell, L. Bocquet, *Nature* **2013**, *494*, 455.

[15] K. Raidongia, J. Huang, *J. Am. Chem. Soc.* **2012**, *134*, 16528.

[16] J. Ji, Q. Kang, Y. F. Zhou, Y. Feng, X. Chen, J. Yuan, W. Z. Guo, Y. K. Wei, L. Jiang, *Adv. Funct. Mater.* **2017**, *27*, 1603623.

[17] J.-J. Shao, K. Raidongia, A. R. Koltonow, J. Huang, *Nat. Commun.* **2015**, *6*, 7602.

[18] S. Qin, D. Liu, G. Wang, D. Portehault, C. J. Garvey, Y. Gogotsi, W. Lei, Y. Chen, *J. Am. Chem. Soc.* **2017**, *139*, 6314.

[19] C. E. Ren, K. B. Hatzell, M. Alhabeb, Z. Ling, K. A. Mahmoud, Y. Gogotsi, *J. Phys. Chem. Lett.* **2015**, *6*, 4026.

[20] J. Feng, M. Graf, K. Liu, D. Ovchinnikov, D. Dumcenco, M. Heiranian, V. Nandigana, N. R. Aluru, A. Kis, A. Radenovic, *Nature* **2016**, *536*, 197.

[21] W. Xin, Z. Zhang, X. Huang, Y. Hu, T. Zhou, C. Zhu, X.-Y. Kong, L. Jiang, L. Wen, *Nat. Commun.* **2019**, *10*, 3876.

[22] C.-N. Yeh, K. Raidongia, J. Shao, Q.-H. Yang, J. Huang, *Nat. Chem.* **2015**, *7*, 166.

[23] S.-O. Tung, S. Ho, M. Yang, R. Zhang, N. A. Kotov, *Nat. Commun.* **2015**, *6*, 6152.

[24] M. Yang, K. Cao, L. Sui, Y. Qi, J. Zhu, A. Waas, E. M. Arruda, J. Kieffer, M. D. Thouless, N. A. Kotov, *ACS Nano* **2011**, *5*, 6945.

[25] S. R. Kwon, J. Harris, T. Zhou, D. Loufakis, J. G. Boyd, J. L. Lutkenhaus, *ACS Nano* **2017**, *11*, 6682.

[26] J. Li, W. Tian, H. Yan, L. He, X. Tuo, *J. Appl. Polym. Sci.* **2016**, *133*, 43623.

[27] Y. Li, S. Yuan, C. Zhou, Y. Zhao, B. Van der Bruggen, *J. Mater. Chem. A* **2018**, *6*, 22987.

[28] Z. Ma, S. Kang, J. Ma, L. Shao, A. Wei, C. Liang, J. Gu, B. Yang, D. Dong, L. Wei, Z. Ji, *ACS Nano* **2019**, *13*, 7578.

[29] C. Chen, D. Liu, L. He, S. Qin, J. Wang, J. M. Razal, N. A. Kotov, W. Lei, *Joule* **2020**, *4*, 247.

[30] Z. Zhang, S. Yang, P. Zhang, J. Zhang, G. Chen, X. Feng, *Nat. Commun.* **2019**, *10*, 2920.

[31] X. Zhu, J. Hao, B. Bao, Y. Zhou, H. Zhang, J. Pang, Z. Jiang, L. Jiang, *Sci. Adv.* **2018**, *4*, eaau1665.

[32] K. Touati, F. Tadeo, T. Schiestel, *Energy Procedia* **2014**, *50*, 960.

[33] A. Alessandrino, B. Marelli, C. Arosio, S. Fare, M. C. Tanzi, G. Freddi, *Eng. Life Sci.* **2008**, *8*, 219.

[34] J. D. van Beek, L. Beaulieu, H. Schäfer, M. Demura, T. Asakura, B. H. Meier, *Nature* **2000**, *405*, 1077.

[35] A. Nakayama, A. Kakugo, J. P. Gong, Y. Osada, M. Takai, T. Erata, S. Kawano, *Adv. Funct. Mater.* **2004**, *14*, 1124.

[36] B. Yang, L. Wang, M. Zhang, J. Luo, X. Ding, *ACS Nano* **2019**, *13*, 7886.

[37] L. Lv, X. Han, L. Zong, M. Li, J. You, X. Wu, C. Li, *ACS Nano* **2017**, *11*, 8178.

[38] D. Lee, B. Lee, K. H. Park, H. J. Ryu, S. Jeon, S. H. Hong, *Nano Lett.* **2015**, *15*, 1238.

[39] C. Chen, Q.-H. Yang, Y. Yang, W. Lv, Y. Wen, P.-X. Hou, M. Wang, H.-M. Cheng, *Adv. Mater.* **2009**, *21*, 3007.

[40] M. Wang, D. Vecchio, C. Wang, A. Emre, X. Xiao, Z. Jiang, P. Bogdan, Y. Huang, N. A. Kotov, *Sci. Rob.* **2020**, *5*, eaba1912.

[41] F. Vollrath, D. P. Knight, *Nature* **2001**, *410*, 541.

[42] Z. Zhang, X. Sui, P. Li, G. Xie, X.-Y. Kong, K. Xiao, L. Gao, L. Wen, L. Jiang, *J. Am. Chem. Soc.* **2017**, *139*, 8905.

[43] A. Esfandiar, B. Radha, F. C. Wang, Q. Yang, S. Hu, S. Garaj, R. R. Nair, A. K. Geim, K. Gopinadhan, *Science* **2017**, *358*, 511.

[44] K. Gopinadhan, S. Hu, A. Esfandiar, M. Lozada-Hidalgo, F. C. Wang, Q. Yang, A. V. Tyurnina, A. Keerthi, B. Radha, A. K. Geim, *Science* **2019**, *363*, 145.

[45] L. Mogg, S. Zhang, G. P. Hao, K. Gopinadhan, D. Barry, B. L. Liu, H. M. Cheng, A. K. Geim, M. Lozada-Hidalgo, *Nat. Commun.* **2019**, *10*, 4243.

[46] L. Mogg, G. P. Hao, S. Zhang, C. Bacaksiz, Y. C. Zou, S. J. Haigh, F. M. Peeters, A. K. Geim, M. Lozada-Hidalgo, *Nat. Nanotechnol.* **2019**, *14*, 962.

[47] H. G. Park, Y. Jung, *Chem. Soc. Rev.* **2014**, *43*, 565.

[48] Z. Zhang, X.-Y. Kong, K. Xiao, Q. Liu, G. Xie, P. Li, J. Ma, Y. Tian, L. Wen, L. Jiang, *J. Am. Chem. Soc.* **2015**, *137*, 14765.

[49] S. Qin, D. Liu, Y. Chen, C. Chen, G. Wang, J. Wang, J. M. Razal, W. Lei, *Nano Energy* **2018**, *47*, 368.

[50] C.-Y. Lin, C. Combs, Y.-S. Su, L.-H. Yeh, Z. S. Siwy, *J. Am. Chem. Soc.* **2019**, *141*, 3691.

[51] J. Gao, W. Guo, D. Feng, H. Wang, D. Zhao, L. Jiang, *J. Am. Chem. Soc.* **2014**, *136*, 12265.

[52] X. Zhu, Y. Zhou, J. Hao, B. Bao, X. Bian, X. Jiang, J. Pang, H. Zhang, Z. Jiang, L. Jiang, *ACS Nano* **2017**, *11*, 10816.

[53] J. Veerman, M. Saakes, S. J. Metz, G. J. Harmsen, *J. Membr. Sci.* **2009**, *327*, 136.

[54] D. A. Vermaas, M. Saakes, K. Nijmeijer, *Environ. Sci. Technol.* **2011**, *45*, 7089.

[55] D. A. Vermaas, M. Saakes, K. Nijmeijer, *J. Membr. Sci.* **2011**, *385–386*, 234.

[56] Y. Zhang, G. C. Schatz, *J. Phys. Chem. Lett.* **2017**, *8*, 2842.